Volume 1, No.1, 1984

Journal of the Faculties of
Engineering of Uludağ University

PREDICTION OF TURBULENT SWIRLING FLOWS IN ANNULI

TAHIR KARASU* and D. BRIAN SPALDING

Department of Mechanical Engineering
Imperial College of Science and Technology
Exhibition Road, London SW7 2BX, England

ABSTRACT

The paper presents the use of a numerical solution procedure for the prediction of steady, incompressible, and two-dimensional axisymmetric turbulent swirling flows in annuli. The mathematical model comprises differential equations for continuity, momentum, turbulence kinetic energy and its rate of dissipation. The simultaneous solution of these equations by means of a finite-difference solution algorithm yields the values of the variables at all internal grid points in the flow domain. The numerical solution procedure, composed of the mathematical model and its solution algorithm, is applied to predict the fields of variables within annular ducts; the results of predictions are compared with published experimental data. The predicted results for turbulent flow in a vertical large-gap annulus with both rotating and non-rotating inner cylinder, and for turbulent swirling flow in a stationary annulus with a rotating inlet were in generally good agreement with experimental measurements reported in the literature.

1. INTRODUCTION

The present study is concerned with the prediction of turbulent swirling flows in annuli using upwind discretisation scheme and the k- ϵ model of turbulence[1,2]. Two types of swirling flow situations have been studied; namely, axisymmetric turbulent flow in a vertical large-gap annulus with rotating inner cylinder, and axisymmetric turbulent swirling flow in a stationary annulus. In addition, turbulent non-swirling flow in a vertical large-gap annulus has also been studied.

A swirling flow in a stationary circular-sectioned duct or annulus combines the characteristics of a vortex motion with axial motion along the duct or annulus. The fluid moves in spiral or helical paths; the direction of the mean velocity changes continuously and varies as a function of position in the flow field. This is a field in which the swirling motion decays and the velocity and pressure distributions develop towards those of a pure axial flow.

---

* *Assistant Professor, Department of Mechanical Engineering, Uludağ University, Bursa, Turkey.*

Considerable experimental and theoretical works on turbulent swirling flows in stationary circular-sectioned ducts and annuli have been reported in the literature. Among the interesting ones are the works of King et al.[3], Murakami et al.[4], Weske and Sturov[5], Sukhovich[6], Yeh[7], Scott and Rask[8], Scott and Bartelt[9], and Murthy and Soehngen[10]. In the present investigation, the experimental data of Scott and Bartelt[9] for turbulent swirling flow in a stationary annulus with a rotating inlet section have been employed for comparison with the predictions.

On the other hand, the swirling flow in an annulus with inner cylinder rotation is different from the one just described above. In this case, both the axial and the swirl velocities develop with distance along the annular duct and attain fully-developed state at certain lengths, after which they do not change with downstream distance.

Experimental studies of turbulent flows in annuli with one or two rotating walls include the works of Taylor[11,12], Zmeykov et al.[13], Bissonnette and Mellor[14], and Lohmann[15]. Turbulent flow in an annulus with rotating inner cylinder has been investigated experimentally by Kuzay[16], and numerically by Sharma et al.[17], who employed the prediction procedure of Patankar and Spalding[18] for the computation of the flow using a mixing-length hypothesis. In the present study, the experimental measurements of Kuzay[16] have been used for comparison with the calculations.

The above-described turbulent flows have been predicted by the use of a mathematical and physical model, which gives the local values of components of velocity, pressure and some useful properties of turbulence. The model comprises a set of non-linear partial differential equations, the simultaneous solution of which by means of a finite-difference solution procedure yields the values of dependent variables at all internal grid points in the flow domain. The Reynolds stresses arising from turbulence have been represented by a two-equation model of turbulence, which entails the solution of two differential equations of transport for kinetic energy of turbulence and its rate of dissipation.

The paper is divided into five sections, of which the present one is the first. The next section, Section 2, presents the equations that govern turbulent flow. These equations are then discretised and the approximation made to model the convective terms is provided for the upwind scheme. The solution procedue is briefly described in Section 3. The results of the predictions for turbulent flows in annuli are presented in Section 4. Finally conclusions drawn from the present study are given in Section 5.

2. THE MATHEMATICAL FORMULATION

2.1. The Governing Equations

The time-averaged equations governing steady, incompressible axisymmetric turbulent swirling flow in the cylindrical coordinate system can be conveniently cast into the following forms.

The continuity equation:

$$\frac{1}{r}\frac{\partial}{\partial r}(\rho r v)+\frac{\partial}{\partial x}(\rho u)=0 \qquad (1)$$

The momentum equations:

r-direction:

$$\rho\left[\frac{1}{r}\frac{\partial}{\partial r}(r v^{2})+\frac{\partial}{\partial x}(uv)\right]=\frac{1}{r}\frac{\partial}{\partial r}\left(r\mu_{eff}\frac{\partial v}{\partial r}\right)+\frac{\partial}{\partial x}\left(\mu_{eff}\frac{\partial v}{\partial x}\right)$$

$$-\frac{\partial p}{\partial r}+\frac{1}{r}\frac{\partial}{\partial r}\left[r\mu_{eff}\frac{\partial v}{\partial r}\right]+\frac{\partial}{\partial x}\left[\mu_{eff}\frac{\partial u}{\partial r}\right]-2\mu_{eff}\frac{v}{r^{2}}+\frac{\rho v_{\theta}^{2}}{r}\;;(2)$$

θ-direction:

$$\rho\{\frac{1}{r}\frac{\partial}{\partial r}[rv(v_\theta r)] + \frac{\partial}{\partial x}[u(v_\theta r)]\} = \frac{1}{r}\frac{\partial}{\partial r}[r^2 \mu_{eff}\, r \frac{\partial}{\partial r}(\frac{v_\theta}{r})]$$

$$+ \frac{\partial}{\partial x}[\mu_{eff}\frac{\partial}{\partial x}(v_\theta r)] \; ; \qquad (3)$$

x-direction:

$$\rho\,[\frac{1}{r}\frac{\partial}{\partial r}(rvu) + \frac{\partial}{\partial x}(u^2)] = \frac{1}{r}\frac{\partial}{\partial r}[r\mu_{eff}\frac{\partial u}{\partial r}] + \frac{\partial}{\partial x}[\mu_{eff}\frac{\partial u}{\partial x}]$$

$$- \frac{\partial p}{\partial x} + \frac{1}{r}\frac{\partial}{\partial r}[r\mu_{eff}\frac{\partial v}{\partial x}] + \frac{\partial}{\partial x}[\mu_{eff}\frac{\partial u}{\partial x}] \qquad (4)$$

where v, v_θ and u are the velocities in the radial (r), tangential (θ) and axial (x) coordinate directions, $v_\theta r$ is the angular momentum, ρ is the fluid density, P is the pressure and μ_{eff} is the effective viscosity defined by equation (8).

2.2. The Turbulence Model

The model employed in the present study is the k-ϵ model of[19], in the form described by[1,2]. It necessitates the solution of two differential equations of transport for two turbulence quantities; namely turbulence kinetic energy, k and its rate of dissipation, ϵ.

The partial-differential equations governing the transport of k and ϵ are given below:

The k-equation:

$$\rho\,[\frac{\partial}{\partial x}(uk) + \frac{1}{r}\frac{\partial}{\partial r}(rvk)] = \frac{\partial}{\partial x}[\Gamma_{eff,k}\frac{\partial k}{\partial x}]$$

$$+ \frac{1}{r}\frac{\partial}{\partial r}[r\Gamma_{eff,k}\frac{\partial k}{\partial r}] + G_k - \rho\varepsilon \qquad (5)$$

where $\Gamma_{eff,k}$ is the effective exchange coefficient for k, defined by equation (9), and G_k which represents the generation rate of turbulence kinetic energy is:

$$G_k = \mu_t\,\{2\,[(\frac{\partial u}{\partial x})^2 + (\frac{\partial v}{\partial r})^2 + (\frac{v}{r})^2] + (\frac{\partial u}{\partial r} + \frac{\partial v}{\partial x})^2 + (\frac{\partial v_\theta}{\partial x})^2$$

$$+ [r\frac{\partial}{\partial r}(\frac{v_\theta}{r})]^2\} \qquad (6)$$

The ϵ-equation:

$$\rho\,[\frac{\partial}{\partial x}(u\varepsilon) + \frac{1}{r}\frac{\partial}{\partial r}(rv\varepsilon)] = \frac{\partial}{\partial x}[\Gamma_{eff,\varepsilon}\frac{\partial \varepsilon}{\partial x}]$$

$$+ \frac{1}{r}\frac{\partial}{\partial r}[r\Gamma_{eff,\varepsilon}\frac{\partial \varepsilon}{\partial r}] + \frac{\varepsilon}{k}(C_1 G_k - C_2\rho\varepsilon) \qquad (7)$$

where C_1 and C_2 are turbulence constants whose values are given in Table 1, and $\Gamma_{eff,\epsilon}$ is the effective exchange coefficient for ϵ, defined by equation (9).

Knowledge of the local values of k and ϵ allows the evaluation of a local effective viscosity, μ_{eff}, from which the turbulent shear stresses are calculated. The effective viscosity, μ_{eff}, is calculated via:

$$\mu_{eff} = \mu_l + \mu_t = \mu_l + C_\mu \rho \frac{k^2}{\epsilon} \tag{8}$$

where ρ and μ_l are respectively the density and molecular viscosity. μ_t and μ_{eff} are respectively the turbulent and effective viscosities. The quantity C_μ is the turbulence model constant. The value of which is given in Table 1.

The effective exchange coefficient, $\Gamma_{eff,\Phi}$, appearing in equations (5) and (7) is defined as:

$$\Gamma_{eff,\Phi} = \frac{\mu}{\sigma_\phi} + \frac{\mu_t}{\sigma_{\phi,t}} \tag{9}$$

where σ_ϕ and $\sigma_{\phi,\,t}$ are respectively the laminar and turbulent Prandtl/Schmidt numbers of the variable Φ.

The laminar Prandtl/Schmidt number, σ_ϕ, is dependent on the molecular properties of the fluid; and is equal to unity for k and ϵ. However, the turbulent Prandtl/Schmidt number, $\sigma_{\phi,\,t}$, is dependent on the turbulence phenomena and its values are given in Table 1, which are the same as those recommended by[2].

Table 1- The Values of the Constants Used in the k-ϵ Turbulence Model

C_μ	C_1	C_2	σ_k	σ_ε
0.09	1.44	1.92	1.0	1.3

2.3. The General Property (Φ) Equation

For future reference, the equations (1), (2), (4), (5) and (7) can be cast into the following general form

$$\rho \left[\frac{1}{r}\frac{\partial}{\partial r}(r\, v\, \Phi) + \frac{\partial}{\partial x}(u\, \Phi)\right] = \frac{1}{r}\frac{\partial}{\partial r}\left[r\Gamma_\Phi \frac{\partial \Phi}{\partial r}\right]$$

$$+ \frac{\partial}{\partial x}\left[\Gamma_\Phi \frac{\partial \Phi}{\partial x}\right] + S_\Phi \tag{10}$$

where Φ stands for any scalar property, and Γ_Φ is the appropriate exchange coefficient for the property Φ, and S_Φ is the source term; it includes all the terms of the Φ-differential equation in question, that belong to neither convection nor the diffusion terms. When Φ equals one, and Γ_Φ and S_Φ equal zero, equation (10) reduces to the continuity equation. When Φ stands for v (or u), and Γ_Φ stands for μ_{eff}, the corresponding momentum equation in the r (or x) direction is obtained. The equations of the turbulence model are obtained when Φ equals k and ϵ, respectively.

2.4. The Wall Functions

In the near-wall region, there is a steep variation in the fluid properties. To avoid the need for detailed calculations in these regions, algebraic relations are employed to relate the values of the dependent variables at a point on the wall to those at a point adjacent to the wall; a logarithmic layer is presumed to exist between these two points.

The wall functions employed in the present study are those recommended by[2], they are:
velocity parallel to wall

$$\frac{U_P}{(\tau_W/\rho)} C_\mu^{1/4} k_P^{1/2} = \frac{1}{\kappa} \mathrm{Ln}\left(E\, y_P \frac{\rho C_\mu^{1/4} k_P^{1/2}}{\mu_1}\right) ; \qquad (11)$$

dissipation rate of turbulence energy

$$\varepsilon_P = \frac{C_\mu^{3/4} k_P^{3/2}}{\kappa\, y_P} \qquad (12)$$

in which U_P, k_P, ϵ_P and y_P are the values of the velocity parallel to the wall, turbulence kinetic energy and dissipation rate of turbulence kinetic energy at a near wall point P, a distance y_P from the wall point w.At the wall point w, the shear stress τ_W, is known or calculable; the constans E and κ are ascribed the values of 9.0 and 0.42 respectively.

2.5. The Finite Difference Discretisation

Equations (1)-(5), (7) and (10) are solved, with their appropriate boundary conditions, by integrating them over finite-difference control volumes that form the physical integration domain considered; an example of the grid arrangement is depicted in Fig. 1 where it is seen that the grid is staggered so that velocity components are located mid-way between the grid points. The angular momentum ($v_\theta r$), pressure, viscosity and any general scalar variable such as turbulence kinetic energy, dissipation rate of turbulence

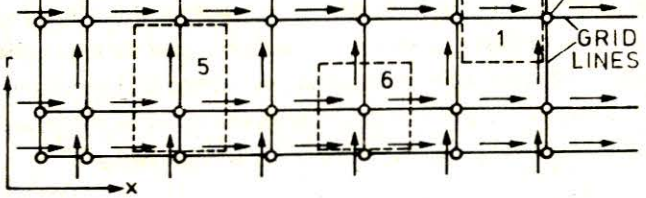

Number	1	2	3	4	5	6
Control Volume Type	U	V	Φ and Continuity	U Boundary	V Boundary	Φ Boundary

Figure 1 — Control volume specification.

kinetic energy are located at the grid points. The main advantage of this arrangement is that the pressure difference between two adjacent grid points becomes the natural driving force for the velocity component located between these grid points. Now, consider a single control volume for Φ, as depicted in Fig. 2; integration of equation (10) over this control volume gives

$$[r\rho u\phi - r\Gamma_\phi \frac{\partial\phi}{\partial x}]_e A_e^\phi - [r\rho u\phi - r\Gamma_\phi \frac{\partial\phi}{\partial x}]_w A_w^\phi$$

$$+[r\rho v\phi - r\Gamma_\phi \frac{\partial\phi}{\partial r}]_n A_n^\phi - [r\rho v\phi - r\Gamma_\phi \frac{\partial\phi}{\partial r}]_s A_s^\phi = S_\phi r_P A_P^\phi \quad (13)$$

where the A's denote cell-face areas at four points (e, w, n, s) located mid-way between the grid points.

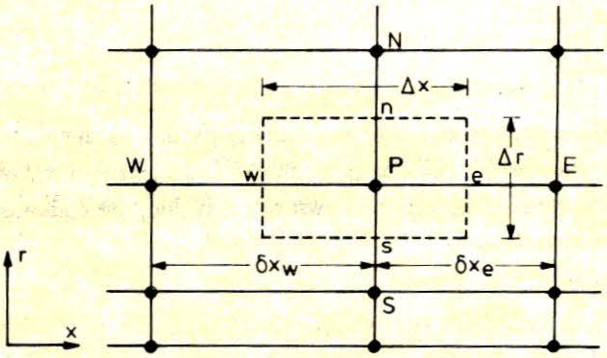

Figure 2 — Control volume for a scalar variable.

The next step in the formulation of a finite-difference equation is the assumption of the variation of ϕ between any two grid points. The diffusion terms are formulated using the central difference scheme; and, since this is common practice, further attention will not be given to them. Attention is given to the convection terms (e.g., the $r\rho u\phi$ terms). Furthermore, the scheme that is used to approximate the convection terms is only applied to convected variable (i.e., ϕ in Eq. (13)); the convecting velocity is discretised using the central-difference scheme.

(i) The Upwind-Difference Scheme

The upwind-difference scheme recognizes that the weak point in the central-difference formulation is the assumption that the convected property ϕ at an interface of the control volume is the average of the ϕ's at the grid points that lie on either side of the interface of the control volume, and proposes a better solution. That is, a piecewise-linear variation of ϕ between grid points is assumed for the diffusive flux, while for the convective flux the value of ϕ convected across an interface is taken to be the value of ϕ at the grid point on the upwind side of the face; for example, when the convective flux is calculated across the west face, w, of the control volume, the value of ϕ_w is expressed as[20-22]:

$$\phi_w = \begin{cases} \phi_W \text{ if } u_w > 0 , \\ \phi_P \text{ if } u_w < 0 . \end{cases} \quad (14)$$

This approximation is adopted chiefly because in the flows to be considered the contribution of the convection to the total flux is dominant. Furthermore, the upwind-difference scheme is not only physically realistic, but also ensures the stability of the solution procedure.

2.6. The Finite Difference Equations

(i) The General Scalar Property (ϕ) Equation

By introducing the above upwind-difference formulation for the ϕ-distributions at the interfaces of the control volume, the finite-difference representation of the general differential equation (10) can be formed. For two-dimensional axisymmetric flow, the finite-difference equation for the general scalar property (ϕ) is of the following form:

$$\phi_P = \frac{C_N^\phi \phi_N + C_S^\phi \phi_S + C_E^\phi \phi_E + C_W^\phi \phi_W + S_u^\phi}{C_N^\phi + C_S^\phi + C_E^\phi + C_W^\phi - S_P^\phi} \tag{15}$$

in which C's are the coefficients which consist of contributions from convection and diffusion, and the S's are components of the source term. The C's are formulated according to the upwind-difference scheme; and it is to those formulations that attention is now turned.

(ii) The Upwind-Difference Scheme

The detailed derivation of the C's for upwind-difference scheme are given in[20]; here the results of manipulating the equations are presented. With reference to Fig. 2, the C's take the forms given below:

$$C_N^\phi = \llbracket D_n^\phi, D_n^\phi - C_n^\phi \rrbracket, \qquad C_S^\phi = \llbracket D_s^\phi, D_s^\phi + C_s^\phi \rrbracket,$$

$$C_E^\phi = \llbracket D_e^\phi, D_e^\phi - C_e^\phi \rrbracket, \qquad C_W^\phi = \llbracket D_w^\phi, D_w^\phi + C_w^\phi \rrbracket \tag{16}$$

in which

$$D_n^\phi = \frac{\Gamma_{\phi,n}\, r_n^\phi\, A_n^\phi}{\delta r_n}, \qquad C_n^\phi = \rho_n\, v_n\, r_n^\phi\, A_n^\phi$$

$$D_e^\phi = \frac{\Gamma_{\phi,e}\, r_e^\phi\, A_e^\phi}{\delta x_e}, \qquad C_e^\phi = \rho_e\, u_e\, r_e^\phi\, A_e^\phi \qquad \text{etc.}$$

The brackets ⟦ ⟧ denote that the C's are assigned the maximum of the values contained within them.

(iii) The Source Term

The source term S_ϕ in equation (10) is integrated over the control volume shown in Fig. 2 and linearised to allow dependence on ϕ_P. The result is:

$$S_\phi\,(r_P \Delta \times \Delta r) = S_u^\phi + S_P^\phi\, \phi_P \tag{17}$$

where S_u^ϕ and Sp^ϕ are two source term coefficients whose composition depends on the particular ϕ-equation considered. Sp^ϕ must be negative to guarantee numerical stability. If there is no real dependence on ϕ_P, then Sp^ϕ is simply set to zero.

(iv) The Momentum Equations

The finite-difference representations of the momentum equations closely resemble the one for the general scalar property (ϕ) equation. However, the control volumes used for the velocity components u and v are different from those of other dependent variables, as illustrated in Fig. 1. Therefore, due allowance is to be made for the staggered locations of the velocities and their control volumes. Also, the pressure gradient term which forms a source of momentum is to be given special attention. With this in mind, the finite-difference forms of the momentum equations may be expressed as follows:

v-momentum

$$[C_N^v + C_S^v + C_E^v + C_W^v - S_P^v]\, v_p = C_N^v\, v_N + C_S^v\, v_S + C_E^v\, v_E + C_W^v\, v_W$$

$$+ r_n \Delta x\,(P_P - P_N) + S_u^v \qquad (18)$$

$v_\theta r$-momentum

$$[C_N^{v_\theta r} + C_S^{v_\theta r} + C_E^{v_\theta r} + C_W^{v_\theta r} - S_P^{v_\theta r}][v_\theta r]_P = C_N^{v_\theta r}[v_\theta r]_N + C_S^{v_\theta r}[v_\theta r]_S + C_E^{v_\theta r}[v_\theta r]_E$$

$$+ C_W^{v_\theta r}[v_\theta r]_W + S_u^{v_\theta r} \qquad (19)$$

u- momentum

$$[C_N^u + C_S^u + C_E^u + C_W^u - S_P^u]u_P = C_N^u\, u_N + C_S^u\, u_S + C_E^u\, u_E + C_W^u\, u_W$$

$$+ r_P \Delta r\,(P_P - P_E) + S_u^u \qquad (20)$$

where the C's are calculated as in equation (16), and S's are the source term coefficients of momentum.

3. THE SOLUTION PROCEDURE

The solution procedure employed to solve the finite-difference equations was the SIMPLE algorithm[23,24]; this algorithm was embodied in the general two-dimensional computer code, called 2/E/FIX, of[25]. In this computer code the finite-difference equations are solved iteratively in a semi-implicit line-by-line fashion using the well-known tri-diagonal matrix algorithm[26]. Due to the semi-implicit nature of the code, under-relaxation factors are employed. A detailed description of the particular solution procedure employed here is presented in[27].

4. THE RESULTS OF THE PREDICTIONS

4.1. Turbulent Flow in an Annulus with Rotating Inner Cylinder

4.1.1. The Physical Situation Considered

In this case the physical situation considered corresponds to the experimental situation of Kuzay[16]. The physical situation and the coordinate system employed for the predictions is sketched in Fig. 3.

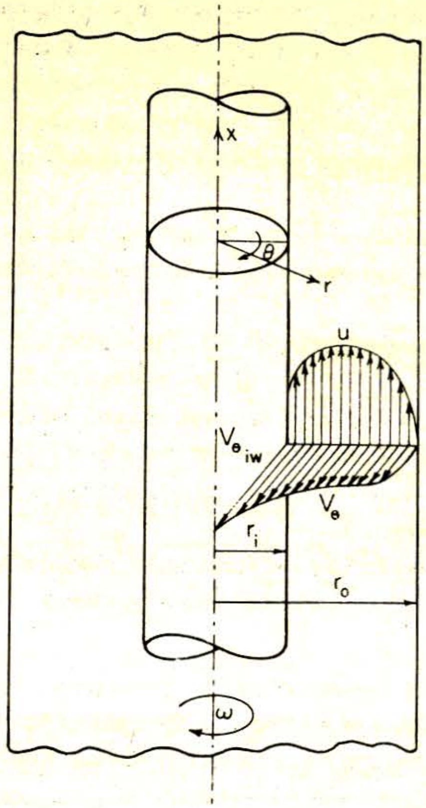

Figure 3 — The physical situation considered.

The vertical annulus of the experimental situation of Kuzay[16] consists of two concentric tubes. The outer tube has an inner diameter of 17.78 cms., while the inner tube has an outer diameter of 10.16 cms. The hydraulic diameter of the annulus, $D_h(=d_o - d_i)$, is 7.62 cms. and the radius ratio (r_i/r_o) is 0.571. The overall length of the annular duct is 50 Dh.

The rotating section begins after the stationary 14 D_h long flow passage over which the axial air flow develops before rotation is imparted on it by the inner tube. Consequently, the swirl velocity profile has 36 D_h for its development length, while the axial velocity profile has 50 D_h. With inner tube rotation, the flow in the annulus is a maintained swirling flow.

4.1.2. Boundary conditions

For the non-swirling flow calculations in the annulus, at the inlet plane (i.e. $x = 0$), a uniform mean axial velocity (u_m) corresponding to the experimental condition was prescribed, while the radial velocity (v) was set to zero. In the absence of any knowledge regarding the distributions of the turbulence quantities k and ϵ at the inlet, initial values were estimated. Fortunately, the calculations are not very sensitive to these initial guesses (see Karasu[27]). The following uniform distributions were prescribed for the turbulence kinetic energy and its rate of dissipation:

$$k = 0.005\, U_m^2 \,, \quad \varepsilon = \frac{C_\mu\, k^{3/2}}{(0.03\, D_h)}$$

where D_h is the hydraulic diameter of the annulus.

For the swirling flow calculations, since the axial flow in the annulus had 14 D_h more of development length then the rotating flow, the distributions of the u, v, k and ϵ quantities at the beginning of rotation, i.e. $x = 14\ D_h$, were those of the non-swirling flow calculations. The angular momentum ($v_\theta r$) was prescribed as zero, because at the entrance to the rotating section only fluid in contact with the rotating wall acquires a swirl velocity; the remaining fluid is swept downstream before angular momentum can diffuse across the annulus.

At the rotating inner wall, the velocity components u and v were set to zero, while the angular momentum ($v_\theta r$) was finite. At the stationary outer wall, the velocity components u, v and angular momentum were all set to zero.

At the exit plane of the annulus, a condition of zero axial gradient was assumed for all dependent variables, i.e. $\partial\phi/\partial x = 0$.

For the components of velocity in the near-wall regions, the specified boundary conditions are the components of the wall-shear stress in the direction of the velocity. This component is identically zero for the velocity component normal to the walls, and are calculated from the wall functions described in Section (2.4) for the other velocity components.

The value of k for a near-wall grid point is calculated from the regular k-balance equation using the wall functions described in Section (2.4), while the value of ϵ is fixed according to Eq. (12).

4.1.3. Some Computational Details

Since the flow in the annulus is axisymmetric, computations were made only for half of the annulus. The finite-difference grid distribution employed in the swirling flow predictions is depicted in Fig. 4. It possesses 17 x 20 grid nodes in the x- and r-directions, respectively. On the other hand, the finite-difference grid used in the non-swirling flow predictions possessed 39 x 20 grid nodes in the x- and r-directions, respectively. The two grids employed were distributed non-uniformly in both x- and r-directions, respectively, with more grid points placed near inner and outer walls of the annulus where steep gradients of dependent variables were expected.

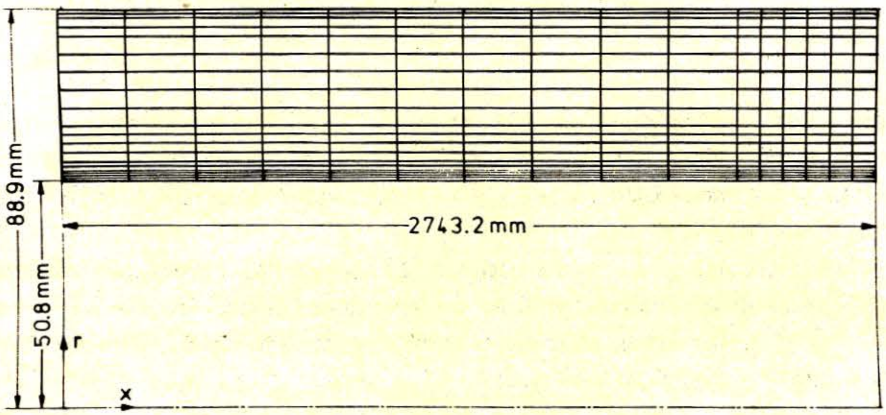

Figure 4 — Finite-difference grid distribution for axisymmetric turbulent flow in an annulus with rotating inner cylinder of Kuzay[16]. Grid size: 17 (x) x 20 (r) points.

As an example, for swirling flow field with Re = 17259 ($Re = \frac{U_m D_h}{\nu}$, where U_m is the mean axial velocity and D_h is the hydraulic diameter of the annulus) and rotation ratio $\zeta = 2.099$ (defined as the ratio of the tangential velocity on the surface of the rotating inner wall to the mean axial velocity in the annulus, i.e. $\zeta = V_{\theta iw}/U_m$), a well-converged solution was attained after 417 iteration cycles of the computational flow domain using 17 x 20 grid size; whereas for swirling flow field Re = 17191 and $\zeta = 2.786$ (Fig. 9), a well-converged solution was achieved after 648 iteration cycles employing the same grid size. On the other hand, for non-swirling flow field with Re = 17327 and $\zeta = 0$ (Fig. 9), a well-converged solution was reached after 140 iteration cycles using 39 x 20 grid size.

The convergence criterion was obtained by specifying that the residuals to each equation, defined by

$$R\phi = \frac{\sum_{\text{all cells}} (\text{convection} + \text{diffusion} + \text{source})}{\text{inlet flux of } \phi}$$

to be less than 10^{-3} for all equations; to obtain this level of convergence required 398 secs. computational time on a CDC 6500 computer for 17 x 20 grid size for swirling flow field with Re = 17259 and $\zeta = 2.099$, and 347 secs. on a CDC 6600 computer for the same grid size for swirling flow field with Re = 17191 and $\zeta = 2.786$, and finally 151 secs. on a CDC 6600 computer for 39 x 20 grid size for non-swirling flow field with Re = 17327 and $\zeta = 0$.

For all the swirling flow fields in the vertical annulus the under-relaxation factors used in the predictions for u, v, $v_\theta r$, k, ϵ, P and μ_{eff} were 0.6, 0.6, 0.6, 0.8, 0.8, 0.5 and 0.5, respectively; and for all the non-swirling flow fields the under-relaxation factors employed in the computations for u, v, k, ϵ, P and μ_{eff} were 0.6, 0.6, 0.8, 0.8, 0.8 and 0.3, respectively. They are not optimised to give the fastest degree of convergence; therefore, experimentation with other sets of under-relaxation factors may result in the reduction of the number of iteration cycles required to obtain a converged solution.

4.1.4. Presentation and Discussion of Results

Figs. 5 to 15 present the results of predictions and their comparisons with the experimental measurements of Kuzay[16] at axial location three hydraulic diameters (3 D_h) below the exit plane of the annulus.

Figs. 5, 7 and 8 show the predicted and measured swirl velocity profiles in dimensionless form $V_\theta/V_{\theta iw}$, and radial position $r - r_i/r_o - r_i$; while Fig. 6 reveals the predicted and measured angular momentum profiles in terms of non-dimensional form $V_\theta r/V_{\theta iw} r_i$, and radial distance $r - r_i/r_o - r_i$. The swirl velocity profiles are made dimensionless with respect to the tangential velocity of the rotating inner wall $V_{\theta iw}$; while the angular momentum profiles are non-dimensionalised by the angular momentum at the rotating inner wall $V_{\theta iw}, r_i$. Both the swirl velocity profiles and the angular momentum profiles are grouped in sets of two at fixed axial Reynolds number. The higher rotation ratio $\zeta = V_{\theta iw}/U_m$ in each set corresponds to nominal 2000 rpm and the lower ζ corresponds to nominal 1500 rpm rotational speeds of the inner cylinder.

Fig. 5 shows that the predicted swirl velocity profiles exhibit similar trends to the measured ones. The latter are over predicted in the inner region of the annulus where dominance of rotation is strong, particularly so near the rotating inner cylinder; however, in the outer region where dominance of rotation is weaker, the predicted profiles are in excellent agreement with the corresponding measured ones. The measured profiles exhibit a free vortex type character only in the mid-region of the annulus. This is particularly observed in the angular momentum profiles in Fig. 6, where the angular momentum ($v_\theta r$) is uniform in approximately 80 % of the annular gap. Near the walls, the measured swirl velocity profiles differ from the free vortex character.

Fig. 7 reveals that the measured profiles are over-predicted in the inner region of the annulus and slightly underpredicted in the outer region, and that the predicted profiles display similar trends to the measured ones. As noticed, at fixed Reynolds number, the agreement obtained between the predicted and measured profiles for case with higher rotation ratio ζ is better than that for case with lower rotation ratio ζ.

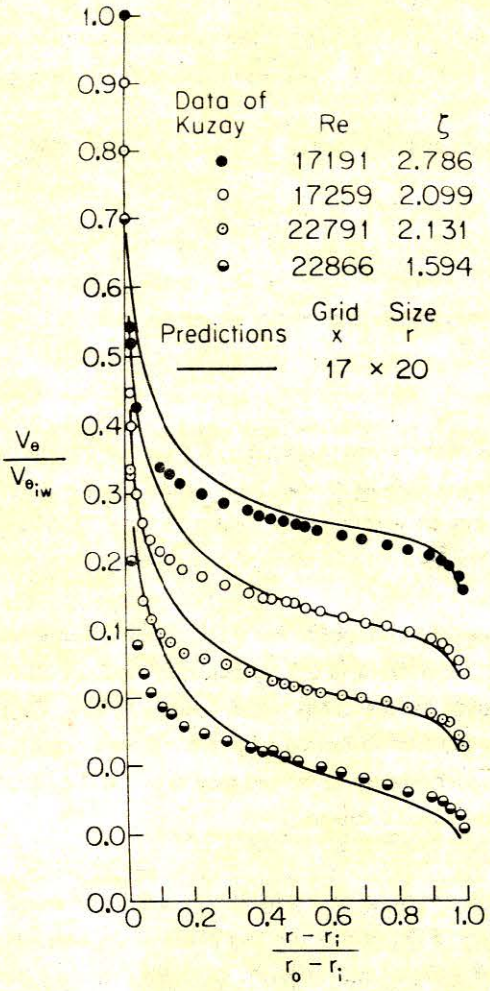

Figure 5 — Comparison between predicted and measured swirl velocity profiles.

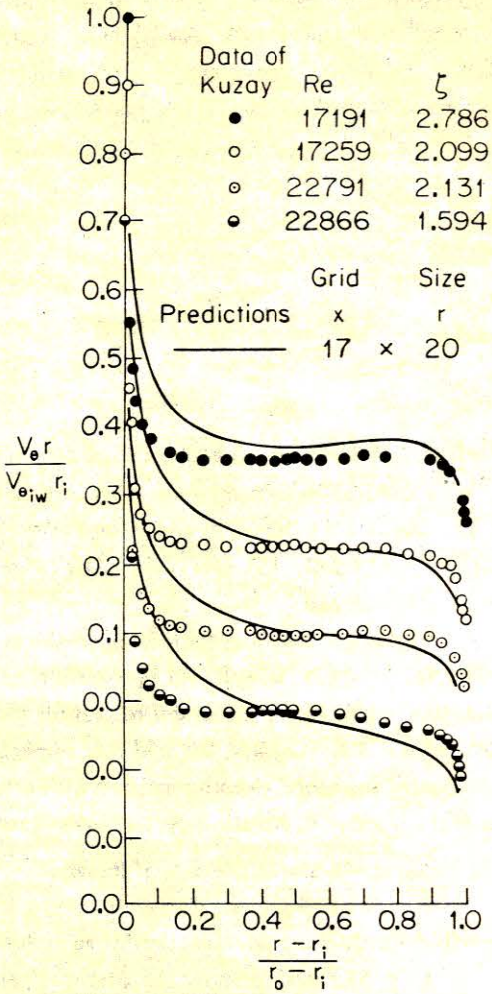

Figure 6 — Comparison between predicted and measured angular momentum profiles.

The reason for this is that the higher the swirl velocity, the larger the turbulent viscosity, and the increased viscosity raises the rate of radial propagation of angular momentum. In this figure the agreement attained between the predicted and measured profiles is not so good as that in Fig. 5.

Fig. 8 shows that the measured profiles are overestimated in the inner region near the rotating inner cylinder and underestimated in the rest of the annular region. However, the predicted profiles exhibit similar trends to the measured ones. The wiggles observed in the measured profiles corresponding to cases with $\zeta = 0.756$ and 0.568 are due to the increased error in the measurement of flow angles, Kuzay[16]. In general, the agreement obtained between the predicted and measured profiles is satisfactory.

Overall examination of Figs. 5 to 8 indicates that as the axial Reynolds number increases the predictions of the swirl velocity profile deteriorate.

The predicted swirl velocity profiles for all rotation ratios (ζ) studied have not attained fully-developed state within the available 36 D_h length of the annular duct. The number of hydraulic diameters required to reach the fully-developed state decreases with increasing rotational velocity of the inner cylinder relative to the mean axial velocity U_m. At low rotation ratios the swirling flow requires greater length to attain the fully-developed state. Accordingly, it seems that, of the Kuzay[16] measurements, only the measurements at the higher rotation ratios have approached the fully-developed state.

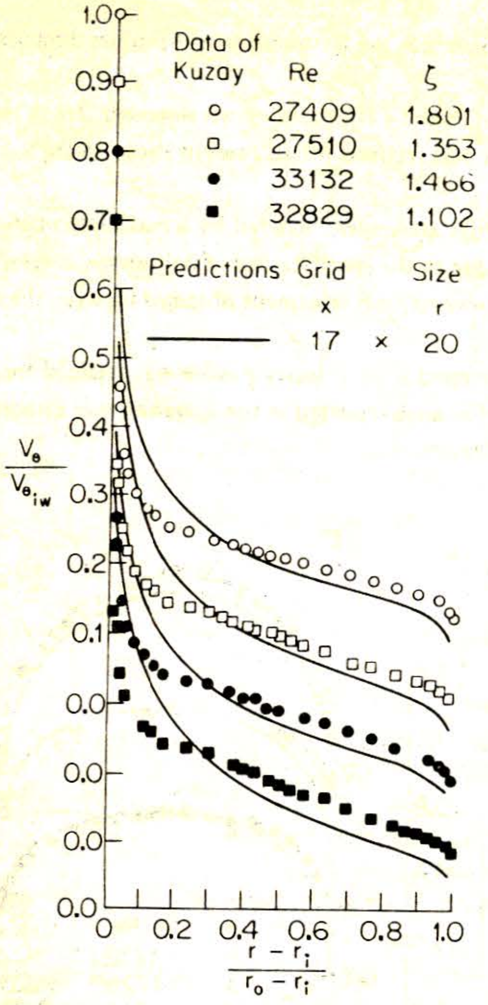

Figure 7 — Comparison between predicted and measured swirl velocity profiles.

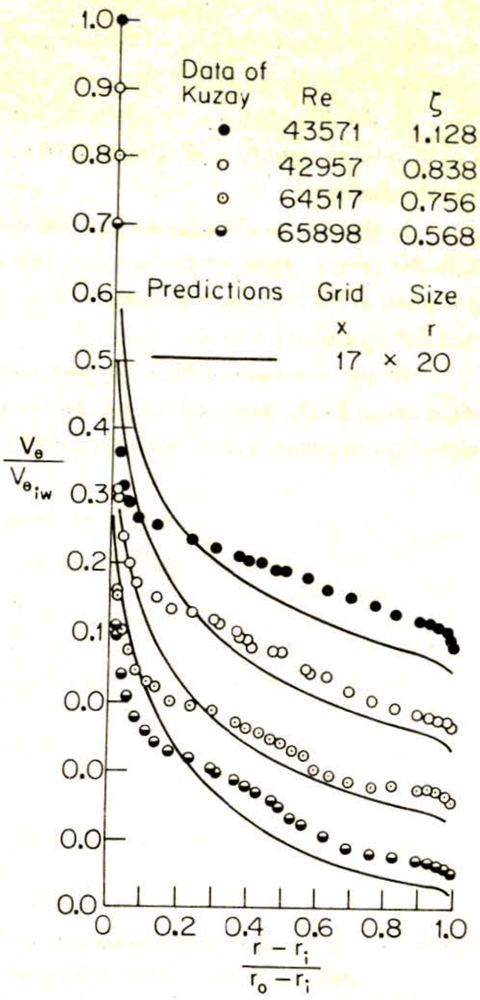

Figure 8 — Comparison between predicted and measured swirl velocity profiles.

Figs. 9 to 14 display the predicted and measured axial velocity profiles in non-dimensional form U/U_m, and radial position $r - r_i/r_o - r_i$, for swirling and non-swirling flow fields in the annulus. These profiles are non-dimensionalised with respect to the mean axial velocity U_m. Each figure presents a set of three profiles at fixed Reynolds number. The highest ζ corresponds to nominal 2000 rpm and the lower ζ corresponds to nominal 1500 rpm rotational speeds of the inner cylinder. The case $\zeta = 0$ represents pure axial flow in the annulus.

Finally, Fig. 15 gives the predicted and measured dimensionless radial profiles of axial velocity for pure axial flow only.

Figs. 9 to 15, which give the comparison between the predicted and measured axial velocity profiles for both swirling and non-swirling flows in the annulus, show generally good agreement between the predicted and measured profiles.

In the swirling flow cases, the measured profiles are appreciably underpredicted in the inner region of the annulus where dominance of rotation is strong; however, in the outer region of the annulus where dominance of rotation is weaker, the predicted profiles are in very good agreement with the corresponding measured ones. In comparison with no-rotation cases, the predicted profiles, like the measured ones, are appreciably flattened owing to rotation in the mid-region of the annulus. This is particularly noticeable in the profiles for $\zeta > 1.5$ in Figs. 9 to 11. As expected, the flattening of the profiles diminishes as rotation ratio ζ decreases.

In the swirling flow calculations, the axial velocity had 14 D_h more of development length than the swirl velocity, and fully-developed axial velocity profile was attained for all cases in about 45 D_h length of the annular duct.

In the non-swirling flow cases, the measured profiles are underpredicted by a maximum of about 4 % in the central region of the annulus. This is probably due to the specification of uniform axial velocity distribution at the inlet plane of the annulus (i.e., $x = 0$). However, the agreement obtained between the predicted and measured profiles is good.

In the non-swirling flow computations, fully-developed axial velocity profile was attained for all cases in about 25 D_h length of the annular duct. This is in the range reported in the literature that turbulent straight flow in annuli will develop between 15 and 30 D_h length.

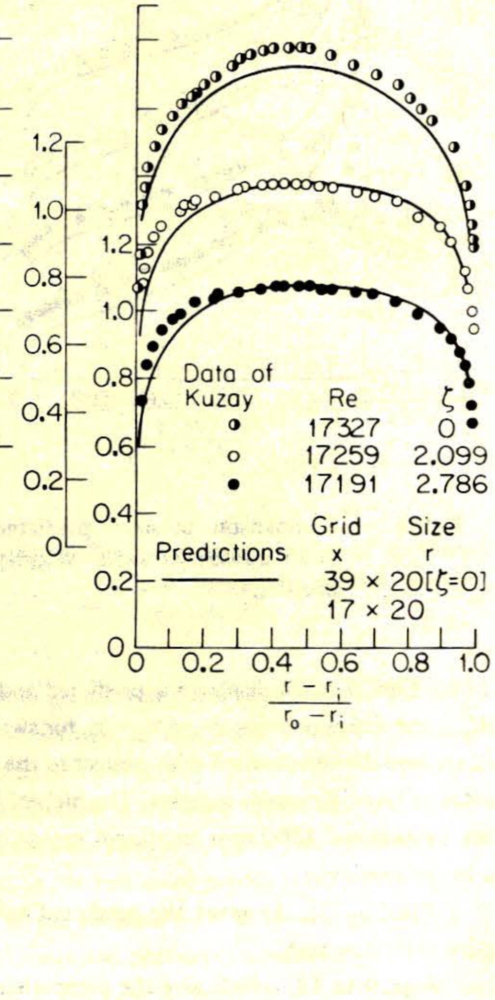

Figure 9 — Comparison between predicted and measured axial velocity profiles.

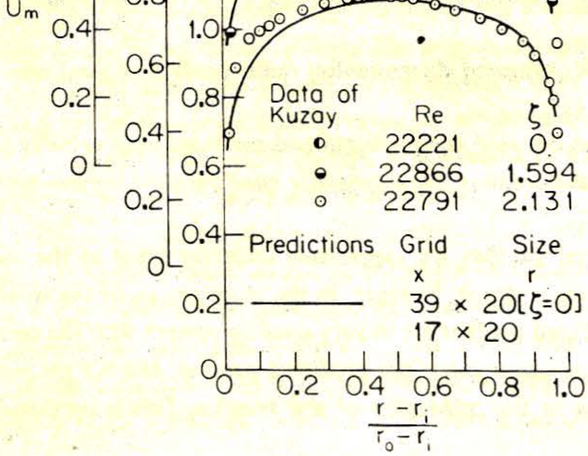

Figure 10 — Comparison between predicted and measured axial velocity profiles.

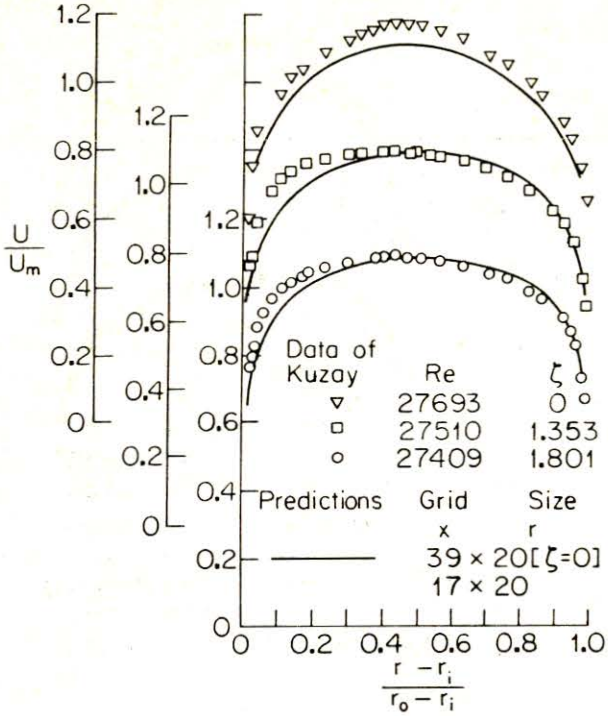

Figure 11 —Comparison between predicted and measured axial velocity profiles.

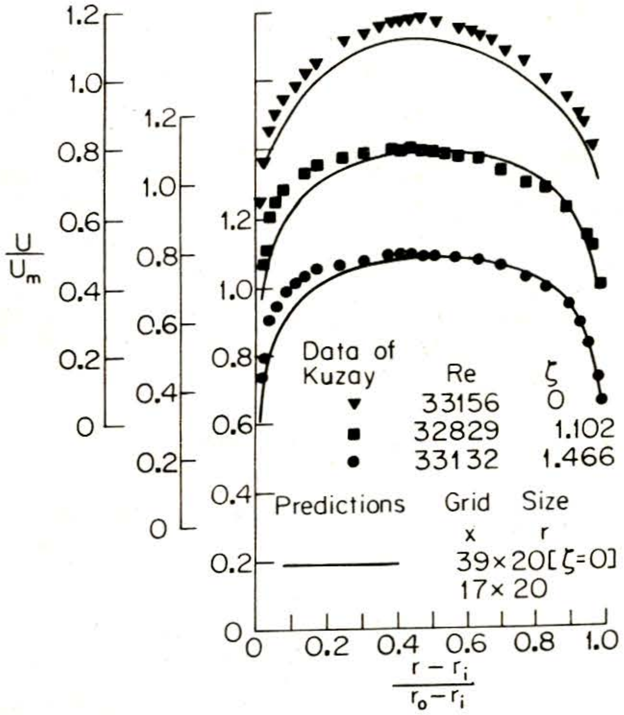

Figure 12 —Comparison between predicted and measured axial velocity profiles.

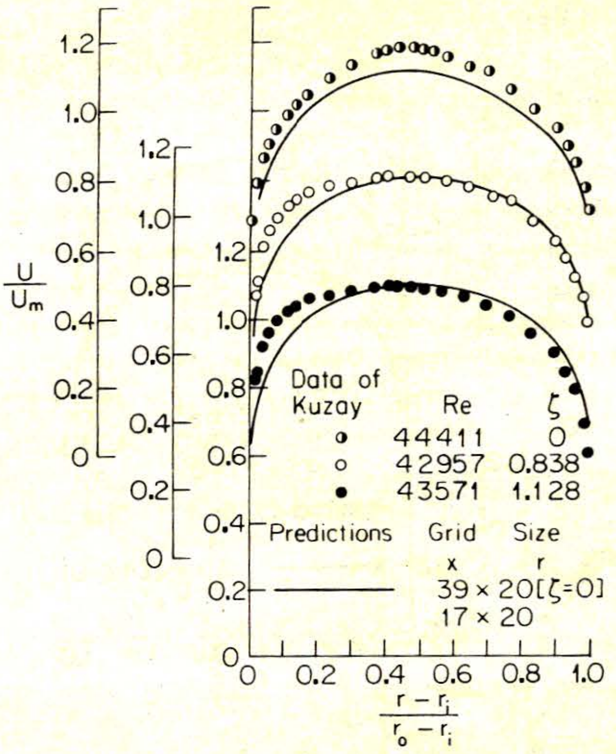

Figure 13 —Comparison between predicted and measured axial velocity profiles.

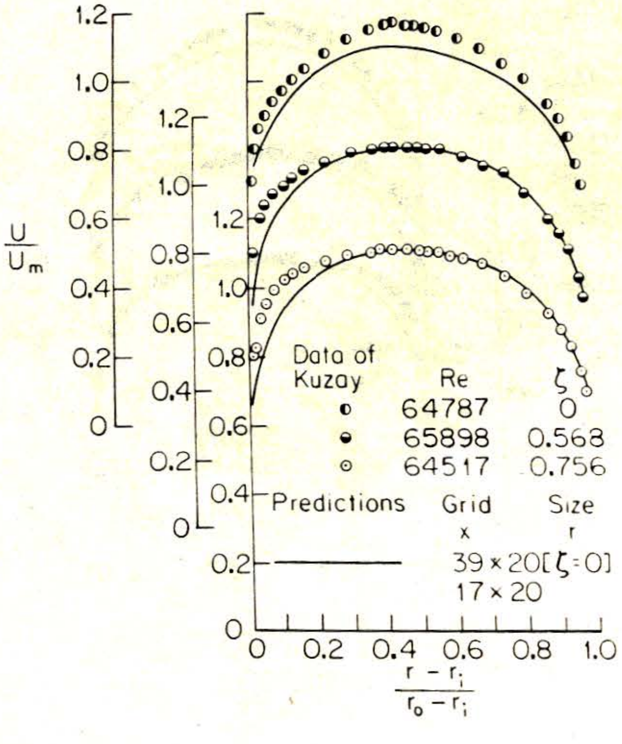

Figure 14 —Comparison between predicted and measured axial velocity profiles.

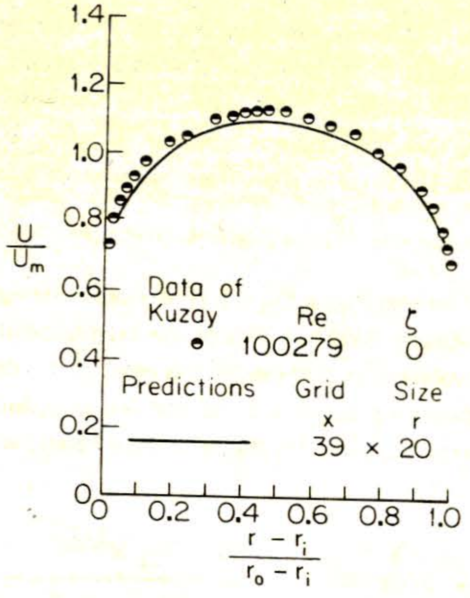

Figure 15 — Comparison between predicted and measured axial velocity profiles.

4.2. Turbulent Swirling Flow in a Stationary Annulus

4.2.1. The Physical Situation Considered

The physical situation and the coordinate system used for the computation of the annular swirl flow is depicted in Fig. 16. It represents the experimental annular test section geometry of Scott and Bartelt[9]. The annular test section of the experimental situation of Scoot and Bartelt[9] consists of two concentric tubes. The outer tube has an inner diameter of 12.7 cms., while the inner tube has an outer diameter of 5.1 cms. The test section is 300 cms. long or 39.3 D_h, where D_h $(= d_o - d_i)$ is the hydraulic diameter of the annulus.

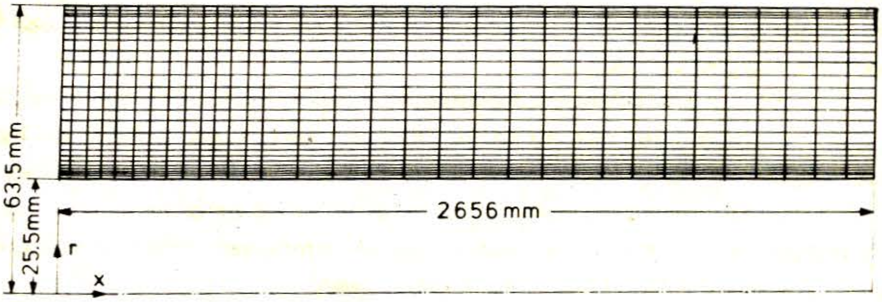

Figure 16 — Finite-difference grid distribution for axisymmetric turbulent swirling flow in a stationary annulus of Scott and Bartelt[9]. Grid size: 33 (x) x 26 (r) points.

In the experimental situation of Scott and Bartelt[9], air enters a rotating inlet section which imparts a swirling motion to it, and then passes through the annular test section; subsequently the air passes through a diffuser, flow straightening tubes, a metering orifice, and finally into a blower which exhausts into the atmosphere.

The rotating inlet section is 15.2 cms. long, and consists of a bundle of parallel tubes, each tube of hexangular cross-section. This honeycomb-like bundle of tubes is of a cylindrical cross-section similar to the annular test section. Air flowing into the honeycomb assumes the rotational velocity of the inlet before entering the test section as a swirling flow. The design is intended, therefore, to provide forced vortex or solid body rotation to the entering fluid. The rotation is provided by means of a variable speed motor whose rpm range is 400-4400.

4.2.2. Boundary Conditions

At the inlet plane of the annulus (i.e., $x/D_h = 1.7$), the experimental profile of angular momentum ($v_\theta r$) and a uniform mean axial velocity corresponding to the experimental condition, i.e. $U_m = 15$ m/sec, were prescribed, while the radial velocity (v) was specified as zero. In the absence of any information regarding the distributions of the turbulence properties k and ϵ at the inlet, initial values were estimated. The following uniform distributions were prescribed for the turbulence kinetic energy and its rate of dissipation:

$$k = 0.02\, U_m^2 \,, \quad \varepsilon = \frac{C_\mu\, k^{3/2}}{(0.03\, D_h)}$$

where U_m is the mean axial velocity, and D_h is the hydraulic diameter of the annulus.

At the inner and outer walls of the annulus, the velocity components u, v and angular momentum ($v_\theta r$) were all set to zero.

At the exit plane, a condition of zero axial gradient was employed for all dependent variables, i.e. $\partial\phi/\partial x = 0$.

As described in sub-section (4.1.2), the turbulence quantities k and ϵ at the near-wall grid points are calculated using the wall functions given in Section (2.4).

4.2.3. Some Computational Details

The computational finite-difference grid distribution used for case with a rotational speed of 3000 rpm of the rotating inlet section of the annulus is shown in Fig. 16. It consists of 33 x 26 grid points in the x- and r-directions, respectively; while the grid employed for case with a rotational speed of 1400 rpm of the rotating inlet section had 33 x 21 grid points in the x- and r-directions, respectively. The two grid sizes employed were distributed non-uniformly in both x- and r-directions, respectively, with more grid points located in the inlet region and near inner and outer walls of the annular duct where steep gradients of dependent variables were expected.

For 33 x 26 grid size, a well-converged solution was obtained after 397 iteration cycles, and the computational time required was 102 secs. on a CDC 7600 computer; where as for 33 x 21 grid size the number of iteration cycles performed was 337, and the computational time needed was 352 secs. on a CDC 6600 computer. Convergence criteria were again chosen as 10^{-3} for each equation.

For the grid sizes quoted above, the under-relaxation factors used in the calculations for u, v, $v_\theta r$, k, ϵ, P and μ_{eff} were 0.6, 0.6, 0.6, 0.8, 0.8, 0.5 and 0.3 respectively.

4.2.4. Presentation and Discussion of Results

The results of computations for turbulent swirling flow in a stationary annulus with a rotating inlet at an average Reynolds number of 72 000 ($Re = U_m Dh/\nu$, where U_m is the mean axial velocity of the flow), and their comparisons with experimental data of Scott and Bartelt[9], are presented in Figs. 17 and 18.

Fig. 17 displays the profiles of angular momentum plotted against the dimensionless radial position $r - r_i/r_o - r_i$, at axial stations $x/D_h = 7$,22.2 and 32.7, for a rotational speed of 3000 rpm of the rotating inlet of the annulus, and reveals that the predicted profiles, like the measured ones, exhibit a uniform axial decay of angular momentum with profile shape independent of axial location. The measured angular momentum profiles exhibit a forced vortex or solid body rotation flow over a major portion of the annular cross-section throughout the length of the annular duct. This forced vortex type flow is also manifested by the predicted angular momentum profiles. Near the outer wall of the annulus, the measured profiles exhibit a free vortex type flow (i.e. $v_\theta r$ = Constant), while the predicted ones do not. The measured profiles are observed to be appreciably overpredicted near the outer and inner walls. However, the agreement obtained between the predicted and measured profiles is generally good.

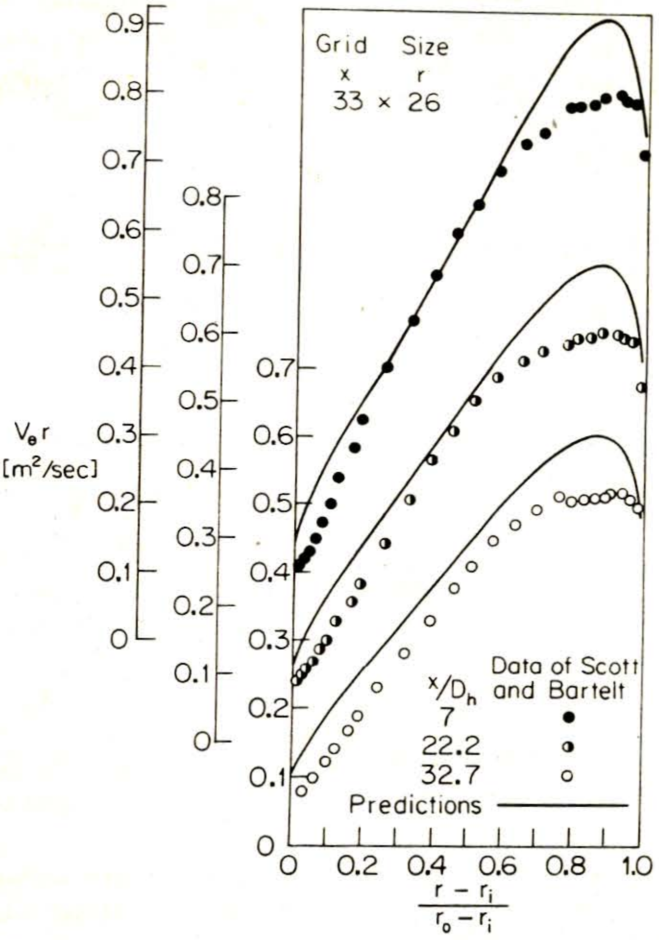

Figure 17 — Comparison of predicted and measured profiles of angular momentum (Inlet rpm = 3000, Re = 72.000).

Fig. 18 shows the profiles of angular momentum plotted against the non-dimensional radial position $r - r_i/r_o - r_i$, at axial stations x/D_h = 7,14.8 and 32.7, for a rotational speed of 1400 rpm of the rotating inlet of the annulus, and reveals that the predicted angular momentum profiles at axial locations x/D_h = 7 and 14.8 are in excellent agreement with the corresponding measured ones. At axial location x/D_h = 32.7, the measured angular momentum profile is appreciably overpredicted over much of the annular cross-section, but the agreement between the predicted and measured profiles is reasonable. Furthermore, it is seen that the measured profiles exhibit a forced vortex character throughout the length of the annular duct; this is satisfactorily demonstrated by the corresponding predicted profiles. Fig. 18 also shows that the predicted profiles, like the measured ones, display a uniform axial decay of angular momentum with profile shape independent of axial location.

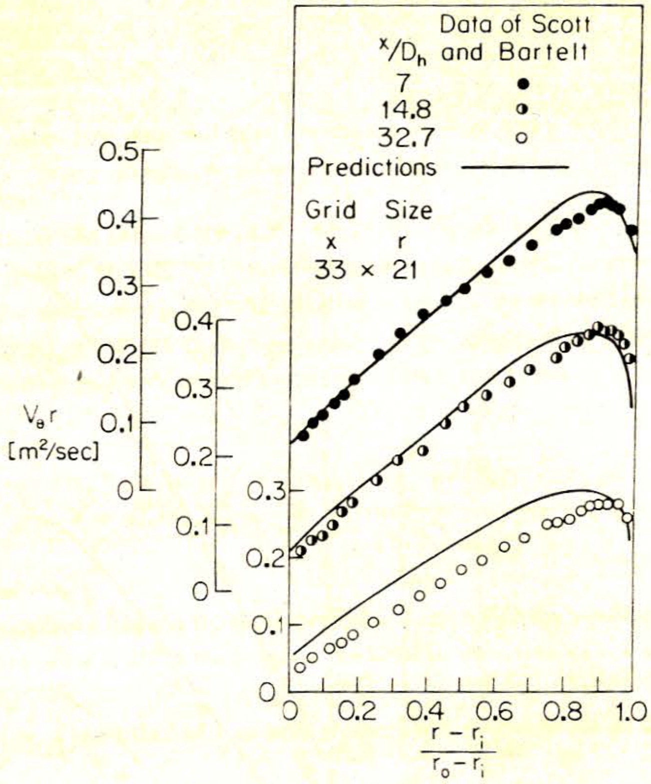

Figure 18 — Comparison of predicted and measured profiles of angular momentum (Inlet rpm = 1400, Re = 72.000).

Comparison of Figs. 17 and 18 shows that:

(i) Both cases exhibit a predominantly forced vortex type flow throughout the length of the annular duct.

(ii) In the case with inlet rotation of 3000 rpm, the region near the outer wall that exhibits a free vortex type flow (i.e. $v_\theta r$ = Constant) is larger than that in the case with inlet rotation of 1400 rpm.

(iii) In both cases, the predicted angular momentum profiles, like the measured ones, exhibit a uniform axial decay of angular momentum with profile shape independent of axial location.

(iv) The discrepancies between the predictions and measurements for the case of inlet rotation of 3000 rpm are much more pronounced than those for the case of inlet rotation of 1400 rpm. This demonstrates that the increased rotation or swirl at the inlet increases the anisotropicity of swirl turbulence in the annulus.

(v) In both cases, the predictions obtained by the use of the k-ϵ turbulence model show generally good agreement with the experimental measurements of Scott and Bartelt[9].

5. CONCLUSIONS

This paper has presented predictions for turbulent flow in a vertical large-gap annulus with both rotating and non-rotating inner cylinder, and for turbulent swirling flow in a stationary annulus with a rotating inlet. The conclusions that can be drawn from this numerical study are as follows.

(i) The predictions made using the k-ϵ turbulence model for both swirling and non-swirling flows in the vertical large-gap annulus were in good agreement with the experimental measurements of Kuzay[16].

(ii) For cases with higher rotation ratio (ζ) and lower axial Reynolds number, the predicted swirl velocity profiles were found to be in better agreement with the corresponding measured ones than those for cases with lower rotation ratio and higher Reynolds number.

(iii) In the swirling flow predictions, the axial velocity, which had 14 hydraulic diameters more of development length than the swirl velocity, attained the fully-developed state in about 45 hydraulic diameters length of the vertical annular duct; while the swirl velocity requires more than 36 hydraulic diameters to reach the fully-developed state. Consequently, it seems that, of the Kuzay[16] measurements, only the measurements at the higher rotation ratios have approached the fully-developed state.

(iv) In the non-swirling flow predictions, the axial velocity attained the fully-developed state in about 25 hydraulic diameters length of the vertical annular duct.

(v) For swirling flow fields in a stationary annulus with a rotating inlet that exhibit predominantly forced vortex or solid body rotation, the predictions obtained employing the k-ϵ turbulence model revealed generally good agreement with the experimental measurements of Scott and Bartelt[9]. The predicted angular momentum profiles, like the measured ones, displayed a uniform axial decay of angular momentum with profile shape independent of axial location.

REFERENCES

1. B.E. Launder and D.B. Spalding; Mathematical Models of Turbulence. Academic Press, London/ New York (1972).
2. B.E. Launder and D.B. Spalding; The numerical computation of turbulent flows. Comp. Meth. Appl. Mech. Engng. 3, 269-289 (1974).
3. M.K. King, R.R. Rothfus and R.I. Kermode; Static pressure and velocity profiles in swirling tube flow. A. I. Ch. E. Journal. 15, 837-842 (1969).
4. M. Murakami, O. Kito, Y. Katayama and Y. Iida; An experimental study of swirling flow in pipes. Bulletin of the JSME. 19, No. 128, 118-126 (1976).
5. D.R. Weske and G.Y. Sturov; Experimental study of turbulent swirled flows in a cylindrical tube. J. Fluid Mechanics-Soviet Research. 3, No. 1,77-82 (1974).
6. Y.P. Sukhovich; Experimental investigation of local properties of swirled turbulent flow in cylindrical channels. J. Fluid Mechanics-Soviet Research. 7, No. 3,74-84 (1978).
7. H. Yeh; Boundary layer along annular walls in a swirling flow. Trans. A.S.M.E. 767-776 (1958).
8. C.J. Scott and D.R. Rask; Turbulent viscosities for swirling flow in a stationary annulus. J. Fluids Engng Trans. A.S.M.E., 557-566 (1973).
9. C.J. Scott and K.W. Bartelt; Decaying annular swirl flow with inlet solid body rotation. J. Fluids Engng Trans. A.S.M.E. 33-40 (1976).
10. S.N.B. Murthy and E.E. Soehngen; Nonisothermal swirling flows in ducts, part 1. Aerospace Research Laboratories ARL 70-0151 (1970).
11. G.I. Taylor; Distribution of velocity and temperature between concentric rotating cylinders. Proceedings of the Royal Society. London, A, 151, 494-512 (1935).
12. G.I. Taylor; Fluid friction between rotating cylinders, part 1: Torque measurements. Proceedings of the Royal Society. London, A, 157, 546-564 (1936).
13. V.N. Zmeykov, B.P. Ustimenko and A.T. Yakovlev; The hydrodynamics and heat transfer of a circular turbulent flow in an annulus formed by two simultaneously rotating cylinders. Heat Transfer-Soviet Research. 2, No: 6, 87-95 (1970).
14. L.R. Bissonnette and G.L. Mellor; Experiments on the behaviour of an axisymmetric turbulent boundary layer with a sudden circumferential strain. J. Fluid Mech. 63, 369-413 (1974).

15. R.P. Lohmann; The response of a developed turbulent boundary layer to local transverse surface motion. J. Fluids Engng Trans. A.S.M.E. 98, 354-363 (1976).

16. T.M. Kuzay; Turbulent heat and momentum transfer studies in an annulus with rotating inner cylinder. Ph. D. Thesis, University of Minnesota (1973).

17. B.I. Sharma, B.E. Launder and C.J. Scott; Computation of annular, turbulent flow with rotating core tube. J. Fluids Engng Trans. A.S.M.E. 753-758 (1976).

18. S.V. Patankar and D.B. Spalding; Heat and Mass Transfer in Boundary Layers. Intertext Books, London (1970).

19. F.H. Harlow and P.I. Nakayama; Transport of turbulence energy decay rate. Los Alamos Scientific Laboratory of the University of California. Report No. LA-3854 (1968).

20. S.V. Patankar; Numerical Heat Transfer and Fluid Flow. McGraw-Hill Book Company, New York (1980).

21. D.B. Spalding; Basic equations of fluid mechanics, and heat and mass transfer, and procedures for their solution. Report No. HTS/76/6, Imperial College, Dept. Mech. Engng., London (1976).

22. D.B. Spalding; A novel finite-difference formulation for differential expressions involving both first and second derivatives. Int. J. Num. Meth. Engng. 4, 551-559 (1972).

23. S.V. Patankar and D.B. Spalding; A calculation procedure for heat, mass and momentum transfer in three-dimensional parabolic flows. Int. J. Heat Mass Transfer. 15, 1787-1806 (1972).

24. L.S. Caretto, A.D. Gosman, S.V. Patankar and D.B. Spalding; Two calculation procedures for steady, three-dimensional flows with recirculation. Proc. 3rd Int. Conf. Num. Methods Fluid Dyn., Paris. II, 60-68 (1972).

25. W.M. Pun and D.B. Spalding; A general computer program for two-dimensional elliptic flows. Report No. HTS/76/2, Imperial College, Dept. Mech. Engg., London (1976).

26. P.J. Roache; Computational Fluid Dynamics, Revised Edn. Hermosa Publishers, New Mexico (1976).

27. T. Karasu, Numerical prediction of incompressible turbulent swirling flows in circular-sectioned ducts and annuli. Ph. D. Thesis, University of London (1981).